Title

Convex gradient optimization for increased spatiotemporal resolution and improved accuracy in phase contrast MRI

Journal

Magnetic Resonance in Medicine, 72(6)

ISSN

0740-3194

Authors

Middione, MJ
Wu, HH
Ennis, DB

Publication Date

2014-12-01

DOI

10.1002/mrm.25059

Peer reviewed

Convex Gradient Optimization for Increased Spatiotemporal Resolution and Improved Accuracy in Phase Contrast MRI

Matthew J. Middione,[1,2] Holden H. Wu,[1,2,3] and Daniel B. Ennis[1,2,3]*

Purpose: To evaluate convex gradient optimization (CVX) for increased spatiotemporal resolution and improved accuracy for phase-contrast MRI (PC-MRI).

Methods: A conventional flow-compensated and flow-encoded (FCFE) PC-MRI sequence was compared with a CVX PC-MRI sequence using numerical simulations, flow phantom experiments, and in vivo experiments. Flow measurements within the ascending aorta, main pulmonary artery, and right/left pulmonary arteries of normal volunteers (N = 10) were acquired at 3T and analyzed using a conventional FCFE sequence and a CVX sequence with either higher spatial resolution or higher temporal resolution. All sequences mitigated chemical shift–induced phase errors and used equivalent breath-hold durations.

Results: Chemical shift–optimized PC-MRI has increased sequence efficiency when using CVX, which can provide either higher spatial or higher temporal resolution compared with conventional FCFE PC-MRI. Numerical simulations, flow phantom experiments, and in vivo experiments indicate that CVX measurements of total flow and peak velocity are increased and more accurate when compared with FCFE.

Conclusion: CVX PC-MRI increases sequence efficiency while reducing chemical shift–induced phase errors. This can be used to provide either higher spatial or higher temporal resolution than conventional chemical shift–mitigated PC-MRI methods to provide more accurate measurements of blood flow and peak velocity. **Magn Reson Med 72:1552–1564, 2014. © 2013 Wiley Periodicals, Inc.**

Key words: phase contrast MRI; convex gradient optimization; flow quantification

INTRODUCTION

Phase-contrast MRI (PC-MRI) is a noninvasive imaging technique that is predominately used clinically to measure two-dimensional (2D) through-plane blood velocity (cm/s) and derived measures such as peak velocity (cm/s), flow rates (mL/s), and flow (mL). PC-MRI flow measurements can guide clinical decision-making in congenital heart disease (1–3), but current clinical confidence in PC-MRI is relatively modest as a consequence of the frequent occurrence of blood flow and velocity results that contradict other clinical observations or are themselves internally inconsistent. Decades of research have helped mitigate numerous sources of PC-MRI measurement error that arise from eddy currents (4), Maxwell terms (5), gradient field distortions (6), and off-resonance (7). Nevertheless, there are still no routine or widespread solutions that correct errors arising from eddy currents, chemical shift–induced phase errors (8), spatiotemporal undersampling (9,10), or physiological variations. Herein, we focus on reducing spatiotemporal undersampling and chemical shift–induced phase errors in PC-MRI.

As a consequence of chemical shift–induced phase errors and suboptimal spatiotemporal resolution, an individual patient's PC-MRI measurements may demonstrate poor intrasubject agreement. For example, an erroneous +5 mL to the right pulmonary artery and −5 mL to the left pulmonary artery makes a normal 60:40 flow split appear to be 2:1 (11), which is an accepted criteria that triggers clinical concern (1). However, if an abnormal flow split is not expected based on other clinical data, this raises concern for all the subject's measurements, calls into question the reliability of the technique, confounds clinical decision-making, and may lead to follow-up examinations, which incur greater downstream costs.

Chemical shift–induced phase errors arise in PC-MRI (8) because the complex signal for perivascular fat chemically shifts across the vessel wall and corrupts the complex blood signal. This error, however, can be mitigated by using an in-phase echo time (TE_{IN}) and a high receiver bandwidth (8). The use of the minimum available TE_{IN} is preferred, but conventional PC-MRI sequences at 3T cannot achieve this short TE ($TE_{IN,MIN} \approx 2.46$ ms at 3T) over a range of clinically relevant velocity encoding strengths (VENCs) (12) because of inefficient gradient waveform design. Hence, existing sequences can only reduce chemical shift–induced errors by using the next longer TE_{IN}, which is longer than TE_{MIN} and compromises sequence efficiency.

Improvements in spatiotemporal resolution for PC-MRI can be achieved in several ways, including alternative k-space sampling trajectories (13–15), parallel imaging (16,17), temporal data sharing schemes (18–20), partial Fourier imaging (21), compressed sensing (22), and k-t acceleration techniques (23). A judicious approach, which is also compatible with all of these methods, is to optimize

[1]Department of Radiological Sciences, University of California, Los Angeles, Los Angeles, California, USA.

[2]Biomedical Physics Interdepartmental Program, University of California, Los Angeles, Los Angeles, California, USA.

[3]Department of Bioengineering, University of California, Los Angeles, Los Angeles, California, USA.

Grant sponsor: Siemens Medical Solutions and the UCLA Department of Radiological Sciences (to D.B.E.); Siemens Medical Solutions (to D.B.E.); The UCLA Department of Radiological Sciences (to D.B.E.).

*Correspondence to: Daniel B. Ennis, Ph.D., 10945 Le Conte Avenue, Ueberroth Building, Suite 1417-B, Department of Radiological Sciences, David Geffen School of Medicine, University of California, Los Angeles, Los Angeles, CA 94305-5488. E-mail: daniel.ennis@ucla.edu

Received 27 August 2013; revised 5 November 2013; accepted 6 November 2013

DOI 10.1002/mrm.25059

Published online 17 December 2013 in Wiley Online Library (wileyonlinelibrary.com).

each gradient waveform such that their duration is minimized, while maintaining the necessary zero and first order gradient moments required for flow imaging. Previously, Bernstein et al. (24) proposed an analytical solution for the construction of asymmetrically weighted velocity-encoding gradients with trapezoidal and triangular gradient lobe shapes to provide a minimum-TE PC-MRI sequence. Bolster and Atalar (25) presented an algorithm to implement three-axis flow-compensation in PC-MRI, which minimized sequence dead time through the construction of trapezoidal and triangular gradient lobe shapes that used the full capabilities of the gradient hardware for any oblique slice orientation. Atalar and McVeigh (26) first introduced hardware-optimized trapezoidal gradient lobes, and Derbyshire et al. (27) later developed hardware-optimized gradients for the slice, phase, and read axes within the physical coordinate system for any oblique slice orientation. Although each of these techniques provide reductions in TE/pulse repetition time (TR) due to more efficient gradient construction, their efficiency is limited due to the required construction of trapezoidal and triangular gradient lobe shapes. This design approach cannot, in general, make optimal use of the available gradient hardware. Most recently, Hargreaves et al. (28) showed that convex gradient optimization (CVX) can be used to minimize gradient waveform durations subject to both gradient hardware and pulse sequence constraints, including the desired gradient moments. This design approach is capable of producing arbitrarily shaped gradient waveforms that cannot be designed analytically.

Herein, we propose, implement, and evaluate a time-efficient (i.e., hardware-optimized) chemical shift–insensitive 2D through-plane PC-MRI sequence that uses an asymmetric velocity-encoding strategy in combination with convex gradient optimization to produce simultaneously the minimum duration gradients for all axes. This sequence mitigates both chemical shift–induced phases errors and spatiotemporal undersampling errors, thereby increasing the accuracy of cardiovascular blood flow and velocity measurements.

THEORY

The design target for a time-efficient PC-MRI sequence is to minimize gradient waveform durations while staying within both sequence and hardware constraints. Sequence constraints arise due to the choice of radiofrequency (RF) pulse duration, slice thickness, field of view (FOV), bandwidth, matrix size, and the required gradient moments for velocity encoding. Additionally, hardware constraints limit the maximum available gradient amplitude, $G_{Max,}$ and slew rate, SR_{Max}. For a time-efficient PC-MRI pulse sequence, two separate CVX optimizations are conducted. First, two slice select gradients (one for each velocity-encoding acquisition), a flow-compensated readout gradient, and a phase-encoding gradient are optimized, simultaneously, for the interval between RF transmission and data acquisition (Interval 1 in Fig. 1b,c). Second, a spoiler gradient, a readout gradient ramp-down, and a phase-encode rewinder gradient are optimized, simultaneously, for the interval between the end of data acquisition and the end of the TR (Interval 2 in Fig. 1b,c). What follows is a description of the velocity-encoding, pulse sequence, and hardware constraints used for the CVX optimization.

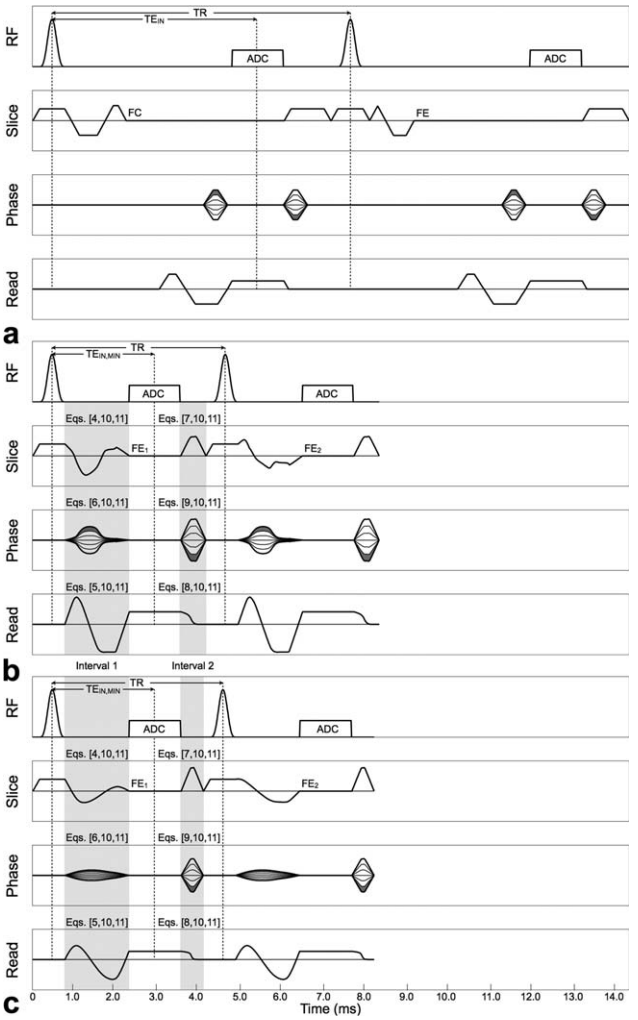

FIG. 1. Pulse sequence diagrams for 2D through-plane chemical shift–mitigated PC-MRI sequences at high bandwidth (814 Hz/pixel) and an in-phase TE (TE_{IN}). **a:** Conventional FCFE velocity-encoded sequence (TE_{IN} = 4.92ms, 1.8 × 1.8mm spatial resolution, 55.9ms temporal resolution). **b:** CVX velocity-encoded sequence optimized for high spatial resolution ($TE_{IN,MIN}$ = 2.46 ms, 1.2 × 1.2 mm spatial resolution, 56.1 ms temporal resolution). **c:** CVX optimized for high temporal resolution ($TE_{IN,MIN}$ = 2.46 ms, 1.8 × 1.8 mm spatial resolution, 31.6 ms temporal resolution). The equations used to constrain the CVX optimization are labeled for each axis. Two separate CVX optimizations are conducted for each sequence as indicated by the gray regions within the pulse sequence diagrams. The two slice select gradients, the flow-compensated readout gradient, and the phase-encoding gradient are optimized during the time between RF transmission and data acquisition (Interval 1). The spoiler, readout ramp-down, and phase encode rewinder gradients are optimized during the time between the end of data acquisition and the end of the TR (Interval 2).

Velocity-Encoding Constraints

For a typical 2D through-plane PC-MRI experiment, two velocity-encoded acquisitions with different first moments are needed to encode flow along the slice

select direction. The velocity-encoding scheme must have a net difference in first moments (M_1) that yields a velocity-dependent phase ($\Delta M_1 = M_{1,1} - M_{1,2} \neq 0$) at TE. The phase difference ($\Delta\varphi$) mitigates the dependence on nonvelocity background phase and is proportional to the velocity (v_z) of flowing blood according to:

$$\Delta\phi = \gamma v_z \Delta M_1. \quad [1]$$

The target ΔM_1 is achieved by acquiring two velocity-encoded acquisitions of the form:

$$M_{1,1} = \alpha \Delta M_1 \quad [2a]$$
$$M_{1,2} = (\alpha\text{-}1)\Delta M_1, \quad [2b]$$

where α scales the first moment distribution and depends on the selected velocity-encoding strategy. Conventionally, velocity-encoding is achieved by using either a pair of equal and opposite bipolar flow encoding gradients ($\alpha = 0.5$) (29,30) or a set of flow-compensated and flow-encoded gradients (FCFE, $\alpha = 0$) (31,32). This requirement is inefficient and typically leads to velocity-encoding gradient waveforms that are unequal in duration. Hence, the minimum achievable TE/TR is limited by the velocity-encoding acquisition with the longest duration. Bernstein et al. (24) used velocity-encoding gradients without constraining α. The only requirement was that the encoding acquisitions produced the required ΔM_1, which results in shorter velocity-encoding gradient waveforms and reductions in TE/TR. We refer to this velocity-encoding strategy as asymmetric velocity-encoding. Herein, we extend this concept and make the gradient waveforms more efficient by starting the velocity-encoding gradients immediately after the slice select gradient plateau, without ramping down. Our CVX PC-MRI sequence is optimized to take full advantage of asymmetric velocity-encoding (flexible α):

$$M_{0,slice,n} = 0 \quad [3a]$$
$$M_{1,slice,1}\text{-}M_{1,slice,2} = \frac{\pi}{\gamma VENC}. \quad [3b]$$

where n is the velocity-encoding step (i.e., 1 or 2).

Pulse Sequence Constraints

The specific pulse sequence protocol defines the end time and gradient amplitude of the slice select gradient and the gradient amplitude and duration of the readout gradient. The velocity-encoding gradient for each encoding step is constructed to begin at the end of the RF pulse and end at the start of data acquisition (Interval 1 in Fig. 1b,c) with the following constraints:

$$G_{slice,n,i} = \frac{2\pi\Delta f}{\gamma\Delta z}, \quad [4a]$$
$$G_{slice,n,f} = 0, \quad [4b]$$

where Δf is the bandwidth of the RF pulse (Hz), γ is the gyromagnetic ratio (MHz/T), and Δz is the slice thickness (m). Therein, i and f indicate the initial and final gradient amplitudes.

The flow-compensated readout gradient is constructed with the following constraints:

$$M_{read,0}(TE) = 0 \quad [5a]$$
$$M_{read,1}(TE) = 0 \quad [5b]$$
$$G_{read,i} = 0 \quad [5c]$$
$$G_{read,f} = \frac{4\pi BW}{\gamma FOV_x}, \quad [5d]$$

where $G_{read,f}$ is the final gradient amplitude for the CVX-optimized flow-compensated readout (mT/m), which is also the readout gradient plateau amplitude; BW is the receiver bandwidth (Hz); and FOV_x is the FOV in the readout direction (m).

The phase-encode gradient is optimized only for the phase-encoding step that requires the largest gradient area, which is equivalently either the largest positive or largest negative phase-encode step for Cartesian k-space acquisitions. Hence, the phase-encoding gradient is designed such that:

$$M_{phase,0} = \frac{\pi(N_y\text{-}1)}{\gamma FOV_y} \quad [6a]$$
$$G_{phase,i} = 0 \quad [6b]$$
$$G_{phase,f} = 0, \quad [6c]$$

where N_y is the number of phase-encoding steps to be acquired and FOV_y is the FOV in the phase encode direction.

Additional constraints are needed for the second interval of CVX optimization (Interval 2 in Fig. 1b,c) for the slice, phase, and read gradients played between the readout gradient plateau and the end of the TR. The spoiler gradient is constructed with the following constraints:

$$M_{spoil,0} = \frac{\varphi}{\gamma\Delta Z} \quad [7a]$$
$$G_{spoil,i} = 0 \quad [7b]$$
$$G_{spoil,f} = 0, \quad [7c]$$

where ψ (rad) is the required phase dispersion of the applied spoiler gradient. The ramp-down of the readout gradient is constructed with the following constraints:

$$G_{read,i} = \frac{4\pi BW}{\gamma FOV_x} \quad [8a]$$
$$G_{read,f} = 0. \quad [8b]$$

The phase-encoding rewinder gradient is designed with the following constraints:

$$M_{rewind,0} = -\frac{\pi(N_y\text{-}1)}{\gamma FOV_y} \quad [9a]$$
$$G_{rewind,i} = 0 \quad [9b]$$
$$G_{rewind,f} = 0. \quad [9c]$$

Gradient Hardware Constraints

In addition to velocity-encoding and pulse sequence constraints, hardware limits (i.e., G_{Max} and SR_{Max}) also constrain sequence design. G_{Max} and SR_{Max} hardware limits, however, may only be reached during a few instances for particular orientations, which unnecessarily limits sequence efficiency. This arises as a consequence of a design strategy that is a holdover from analytical

solutions and hand-coded gradient waveform designs that use simple trapezoidal and triangular gradient lobe shapes. PC-MRI sequences can be made significantly more time-efficient by optimizing the use of the available gradient hardware to jointly design velocity-encoding, phase-encoding, prewinder, rewinder, and spoiler gradients.

For the CVX PC-MRI sequence, the optimization of the gradients during Interval 1 are constrained for each time point according to:

$$\sqrt{max(G_{slice,n}^2) + G_{read}^2 + G_{phase}^2} \leq G_{Max} \qquad [10]$$

where $G_{slice,n}$ represents the gradient amplitudes for the pair of velocity-encoding gradients and G_{read} and G_{phase} represents the gradient amplitudes for the flow-compensated phase-encode gradient and the readout gradient, respectively. Additionally, the slew rates are constrained by replacing G_{Max} with SR_{Max} throughout Equation [10]. Similarly, the optimization of the gradients during Interval 2 are constrained for each time point according to:

$$\sqrt{G_{spoil}^2 + G_{read}^2 + G_{rewind}^2} \leq G_{Max} \qquad [11]$$

where G_{spoil}, G_{read}, and G_{rewind} represent the gradient amplitudes for the spoiler gradient, the ramp-down of the readout gradient, and the phase-encode rewinder gradient, respectively. Similarly, the slew rates are constrained by replacing G_{Max} with SR_{Max} throughout Equation [11].

Minimum-Time Solution

As described by Hargreaves et al. (28), the minimum-time solution for any constrained gradient waveform involves finding the minimum gradient duration, T ($T = m\tau$, where m is an integer and $\tau = 10$ μs, which is the gradient raster time), which produces a solution to the constrained problem. This convex problem can be solved reliably by successive binary searches to divide the interval containing T on each function call. An initial estimate of the upper and lower bounds, T_u and T_l, are defined to start the optimization. For the $TE_{IN,MIN}$ protocols used in this study, T_u and T_l were set to 1.54 ms, based on the target of $TE_{IN,MIN}$ = 2.46 ms minus half the slice select (0.3 ms) and readout (0.62 ms) gradient plateau durations.

For TE_{MIN} protocols, which were not used in this study, T_u can be determined analytically using conventional trapezoid and triangle gradient waveforms and an analytic solution similar to that proposed by Bernstein et al. (24) (Appendix). T_l is then assigned as $T_l = 0.8\ T_u$. The value of T is set to T_u to determine whether the aforementioned constraints are satisfied for all axes, simultaneously. Once a feasible solution exists within the interval of T_u and T_l, T is set to 0.5 ($T_u + T_l$), tested based on the assigned constraints, and then repeated until the minimum feasible T is determined.

Table 1
Gradient Waveform Parameters for FCFE and CVX PC-MRI

	FCFE	CVX Spatial Resolution	CVX Temporal Resolution
Gradient hardware			
G_{Max}, mT/m	23	38[a]	38[a]
SR_{Max}, T/m/s	115	170[a]	170[a]
Velocity-encoding			
G_i, mT/m	0	15.66	15.66
G_f, mT/m	0	0	0
$M_{0,1}$, $M_{0,2}$, mT/m × ms	0, 0	0, 0[b]	0, 0[b]
$M_{1,1}$, $M_{1,2}$, mT/m × ms^2	0, 7.83	1.55, 9.38[b]	2.09, 9.92[b]
Flow-compensated readout			
G_i, mT/m	0	0[c]	0[c]
G_f, mT/m	0	16.45[c]	10.79[c]
M_0, mT/m × ms	0	0[d]	0[d]
M_1, mT/m × ms^2	0	0[d]	0[d]
Phase-encode/rewinder			
G_i, mT/m	0	0[e]	0[e]
G_f, mT/m	0	0[e]	0[e]
M_0, mT/m × ms	± 7.37	± 10.27[e]	± 7.37[e]
Spoiler			
G_i, mT/m	0	0[f]	0[f]
G_f, mT/m	0	0[f]	0[f]
M_0, mT/m × ms	27.86 (9π)	12.57 (4π)[f]	12.57 (4π)[f]
M_1, mT/m × ms^2	90.78	30.18	29.26

[a]Equations 10, 11.
[b]Equation 4a.
[c]Equations 5a, 8a.
[d]Equation 5a.
[e]Equations 6a, 9a.
[f]Equation 7a.

METHODS

Convex Gradient Optimization

$TE_{IN,MIN}$ cannot be achieved with the conventional FCFE PC-MRI sequence, which uses the next available in-phase TE: TE_{IN} = 4.92 ms. The CVX PC-MRI pulse sequence allows the use of $TE_{IN,MIN}$ = 2.46 ms at 3T. In addition, CVX can be used to either reduce scan time or increase spatiotemporal resolution for a fixed breath-hold time compared with conventional FCFE. Therefore, two CVX chemical shift–insensitive PC-MRI protocols were compared with a conventional chemical shift–insensitive FCFE PC-MRI sequence.

Table 1 shows the gradient hardware and pulse sequence constraints used for the CVX sequences. Table 2 shows the PC-MRI sequence parameters used for the chemical shift–insensitive FCFE sequence and the chemical shift–insensitive CVX sequences with optimized spatial and temporal resolution, and Figure 1 shows the corresponding pulse sequence diagrams. Based on our previous work involving the analysis of time-efficient gradient spoiling in PC-MRI (33), the CVX sequences used 4π dephasing for the slice select spoiler gradient compared with FCFE, which uses 9π dephasing.

The CVX optimization was conducted offline using MATLAB (MathWorks, Natick, Massachusetts, USA;

Table 2
PC-MRI Parameters

	FCFE	CVX Spatial Resolution	CVX Temporal Resolution
TE/TR, ms	4.92/7.00	2.46/4.00	2.46/3.95
Temporal resolution, ms	55.9	56.1	31.6
VENC, cm/s	150	150	150
Parallel acceleration		Rate 2 GRAPPA with 24 reference lines	
Flip angle	30°	30°	30°
Segments	4	7	4
FOV, mm	340 × 255	340 × 255	340 × 255
Pixel number	192 × 144	288 × 216	192 × 144
Pixel size, mm	1.8 × 1.8	1.2 × 1.2	1.8 × 1.8
Bandwidth, Hz/pixel	814	827	814
Duration, heartbeats	23	20	23
Acquired cardiac phases[a]	13–18	13–18	23–32

[a]The number of acquired cardiac phases is heart rate–dependent.

code available upon request) and a freely available MATLAB-based modeling system for disciplined convex optimization (34,35). The resulting CVX gradients for PC-MRI were then exported to a text file, which was read within the pulse sequence environment to construct the gradients.

PC-MR Imaging

All imaging was performed on a Siemens Trio 3T system (Siemens Medical Solutions, Erlangen, Germany) using a spoiled gradient echo sequence capable of 40 mT/m maximum gradient amplitude and 200 T/m/s maximum slew rate. The sequence was coded with a G_{Max} = 38 mT/m SR_{Max} = 170 T/m/s to avoid overanging the gradients and potential peripheral nerve stimulation effects. For all experiments, PC-MRI data were acquired using an anterior six-element body matrix coil and a posterior six-element spine matrix coil for signal reception. All imaging was performed with the imaging slice centered at isocenter, as previously recommended for the reduction of velocity offset errors (36).

Numerical Simulations of Spatiotemporal Sampling

The effect of spatiotemporal resolution on PC-MRI total flow and peak velocity measurements was evaluated using a numerical simulation. A 400-ms half sine wave temporal velocity waveform was modeled with 1 ms temporal sampling. The peak velocity was set to 150 cm/s. A 20-mm simulated vessel was constructed with 0.1-mm spatial resolution and a laminar flow profile across the vessel. The velocity profile was sampled with a range of temporal resolutions (30 ms to 100 ms in increments of 10 ms) and temporal offsets (0 ms to the simulated temporal resolution in increments of 10 ms) as well as a range of spatial resolutions (1 × 1 mm to 2.2 × 2.2 mm in increments of 0.1 × 0.1 mm) and spatial offsets (0 × 0 mm to the simulated spatial resolution in increments of 0.1 × 0.1 mm). Note that this simulation was used to analyze the effects of partial volume and temporal filtering through changes in spatial and temporal sampling and did not take into account the MRI signal properties such as flip angle, TE/TR, T_1/T_2, or noise.

Flow Phantom Experiments

Validation of the CVX sequence was performed by comparing flow phantom measurements to the conventional FCFE sequence using identical scan parameters: TE/TR = 3.08/5.08 ms; matrix = 320 × 221; acquisition voxel = 1.5 × 1.5 × 5 mm; flip angle = 30°; receiver bandwidth = 801 Hz/pixel; four views per segment (37); total scan time = 21 heartbeats; temporal resolution = 40.6 ms, 25 cardiac phases reconstructed during a simulated 1000-ms heartbeat; retrospective ECG gating; rate-2 GRAPPA (16) parallel imaging with 24 reference lines; and VENC = 150 cm/s. PC-MRI data were acquired in a sealed tube (20/1.0 mm inner diameter/wall thickness) containing blood-mimicking fluid (40% glycerol, 60% water), which was circulated through the phantom by a CardioFlow 1000MR computer-controlled displacement pump (Shelley Medical Imaging Technologies, Toronto, Ontario, Canada). The flow profile was programmed for two sine waves with peak velocities of 75 and 150 cm/s. Measurements were repeated three times for each sequence at each flow rate. Additionally, flow phantom measurements were obtained using the FCFE and were compared with the higher spatial and higher temporal resolution CVX sequences described in Figure 1 and Tables 1 and 2. The flow profile, designed to match the numerical simulations, consisted of a 400-ms half sine wave with a peak velocity of 150 cm/s. Three measurements for each sequence were acquired.

Sequence Comparison

TE_{MIN} and TR_{MIN} were computed over a range of VENCs for high temporal resolution and high spatial resolution protocols and otherwise fixed parameters (FOV = 340 × 255 mm; receiver bandwidth = 814 Hz/pixel; slice thickness = 5 mm; RF pulse duration = 600 μs) for CVX and asymmetric velocity-encoding with 4π gradient spoiling and for FCFE and bipolar with 9π gradient spoiling.

Preclinical Evaluation in Normal Volunteers

A preclinical evaluation was performed to compare the measurement accuracy for our proposed CVX sequences compared with the conventional FCFE sequence using a chemical shift–insensitive protocol (Fig. 1 and Tables 1 and 2). Our university's Institutional Review Board approved the study and informed consent was obtained for each subject prior to MRI scanning. PC-MRI data were acquired for the ascending aorta, main pulmonary artery, and right and left pulmonary arteries of 10 normal volunteers (3 female, 7 male; age, 26.7 ± 3.6 y) with no previous history of cardiovascular disease.

The imaging plane for ascending aorta flow was located in the ascending aorta distal to the aortic valve and coronary ostia. The imaging plane for flow in the main pulmonary artery was located downstream from the pulmonary valve and proximal to the first bifurcation. The imaging planes for the right and left pulmonary arteries were located ~1 cm distal to the pulmonary bifurcation. All imaging planes were prescribed on bSSFP cine images during end-systole using end-expiratory breath-holds.

Eddy Current Correction

Eddy current–induced velocity offsets were measured by imaging a stationary viscous gel phantom (97.85% water, 2% hydroxyethyl cellulose, 0.1% copper sulfate, and 0.05% sodium azide) placed at the isocenter with identical slice prescriptions and imaging parameters as the PC-MRI scans (4). Stationary phantom correction was conducted within 1 week of all PC-MRI experiments to avoid temporal drift of eddy current–induced phase shifts (38).

Image Processing

Data were processed offline using MATLAB and a DICOM viewing tool (OsiriX; Pixmeo, Geneva, Switzerland). For quantitative flow assessment at each vessel territory, the stationary eddy current correction phantom images were subtracted from the volunteer PC-MRI phase images on a pixel-by-pixel basis. A region-of-interest (ROI) was drawn in OsiriX around the contours of each vessel boundary as indicated in the magnitude images. The resulting ROIs were then imported to the eddy current corrected PC-MRI phase images, which were then exported from OsiriX to MATLAB for quantitative velocity and flow analysis. Measurements of total flow were computed by scaling the mean ROI signal intensity (velocity-related phase shift) by VENC/π (cm/s). The resulting mean ROI velocities were then multiplied by the area of the ROI (cm^2) to calculate the flow rate (mL/s) and finally integrated over the cardiac cycle to yield the total flow results (mL). Measurements of peak velocity were computed by scaling the ROI signal by VENC/π (cm/s) in the cardiac frame with the maximum signal intensity. Measurements of pulmonary to systemic blood flow ratios (Qp/Qs) were computed by dividing measurements of main pulmonary artery total flow by ascending aorta total flow. Measurements of eddy current-induced velocity offsets were computed by scaling the mean ROI signal intensity in each cardiac frame by VENC/π (cm/s) and then averaging across all cardiac frames.

Data Analysis

All statistical analysis was performed in MATLAB. Bland-Altman (39) analysis was used to compare the measurement bias (mean difference between the measurements) and limits of agreement (95% confidence intervals [CI]) between measurements made with FCFE and CVX in addition to comparisons of repeated measurements made with FCFE versus FCFE and CVX versus CVX. The mean and standard deviation of total flow, peak velocity, and eddy current–induced velocity offsets were calculated for each flow territory across the population of volunteers for FCFE and CVX. Additionally, the mean and standard deviation of Qp/Qs were compared for FCFE and CVX. A paired *t* test with Holm-Sidak post hoc correction was used to measure the statistical significance of measurements obtained using FCFE and CVX at the 95% significance level ($P < 0.05$). Lastly, an analysis of sequence efficiency, defined as the ratio of the readout duration and the TR (40,41), was computed for FCFE and CVX.

RESULTS

Numerical Simulations of Spatiotemporal Sampling

Figure 2 shows numerical simulations of the measured total flow and peak velocity for a range of spatial and temporal resolution combinations. The results indicate that the parameters used in the FCFE protocol can lead to a 14.2% error in total flow and a 6.7% error in peak velocity. CVX with high spatial resolution leads to a 10.2% error in total flow and a 6.2% error in peak velocity. CVX with high temporal resolution leads to a 10.5% error in total flow and a 5.9% error in peak velocity.

Flow Phantom Experiments

The Bland-Altman plots and statistics (Fig. 3) show a low measurement bias of 0.28 cm/s (95% CI: −7.14 to 7.69 cm/s) when comparing FCFE and CVX PC-MRI with matched sequence parameters. For reference, comparisons of repeated FCFE experiments had a measurement bias of −0.40 cm/s (95% CI: −4.71 to 3.90 cm/s), and CVX experiments had a measurement bias of −0.65cm/s (95% CI: −4.58 to 3.27 cm/s). Flow phantom measurements of total flow were 85.6 ± 2.3 mL for FCFE, 91.5 ± 1.6 mL for the CVX with high spatial resolution, and 90.9 ± 1.4 mL for CVX with high temporal resolution. Flow phantom measurements of peak velocity were 132.3 ± 2.2 cm/s for FCFE, 135.3 ± 1.6 cm/s for CVX with high spatial resolution, and 137.1 ± 1.7 cm/s for CVX with high temporal resolution.

Sequence Comparison

Figure 4 shows that CVX provides the shortest TE_{MIN} and TR_{MIN} for every VENC compared with FCFE, bipolar, and asymmetric protocols. For the prescribed pulse sequence parameters (see Methods) CVX optimized for high temporal resolution enables the use of $TE_{IN,MIN}$ =

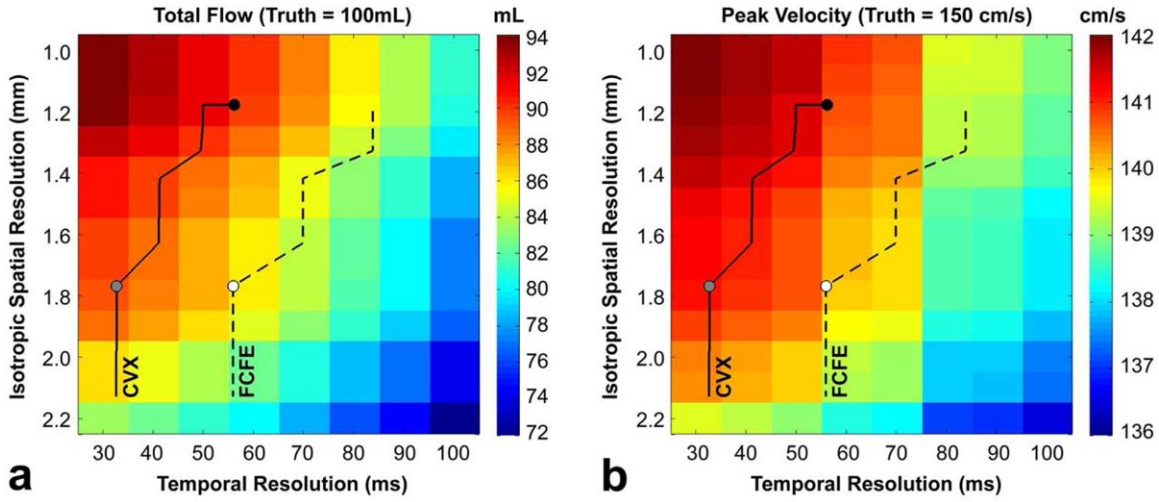

FIG. 2. Numerical simulations of spatiotemporal sampling showing (**a**) the measured total flow and (**b**) peak velocity for different combinations of spatial and temporal resolution. Overlaid on top of the simulations are FCFE (dashed line) and CVX (solid line) contours for chemical shift–insensitive protocols with 20–23 heartbeat scan durations. The PC-MRI sequences described in Table 2 and Figure 1 are denoted by the white (FCFE), black (CVX with high spatial resolution), and gray (CVX with high temporal resolution) circles. The FCFE protocol leads to a 14.2% error in total flow and a 6.7% error in peak velocity. The CVX protocol optimized for high spatial resolution leads to a 10.2% error in total flow and a 6.2% error in peak velocity. The CVX protocol optimized for high temporal resolution leads to a 10.5% error in total flow and a 5.9% error in peak velocity. The simulated total flow and peak velocity were 100 mL and 150 cm/s, respectively.[Color figure can be viewed in the online issue, which is available at wileyonlinelibrary.com.]

2.46 ms for VENCs $\geq$44 cm/s. Comparatively, $TE_{IN,MIN}$ can only be achieved using asymmetric velocity-encoding for VENCs $\geq$ 80 cm/s, whereas FCFE and bipolar cannot achieve $TE_{IN,MIN}$ using this protocol. CVX optimized for high spatial resolution enables the use of $TE_{IN,MIN}$ = 2.46 ms for VENCs $\geq$130 m/s, whereas FCFE, bipolar, and asymmetric velocity-encoding cannot achieve $TE_{IN,MIN}$.

Preclinical Evaluation in Normal Volunteers

Measurements of total flow and peak velocity are listed in Table 3 and are shown in Figure 5, which illustrates that the measurements of total flow and peak velocity were higher for both CVX protocols compared with FCFE in every volunteer and every region. The measured total flow and peak velocity for FCFE versus CVX with high spatial resolution and FCFE versus CVX with high temporal resolution were significantly different ($P < 0.05$). Across all volunteers and vessels, CVX with high spatial resolution resulted in an 8.1% and 3.8% increase in the measured total flow and peak velocity, respectively, compared with FCFE. Similarly, CVX with high temporal resolution increased these same measures by 5.1% and 10.5%. The measured Qp/Qs ratios for FCFE versus CVX with high spatial resolution (1.03 $\pm$ 0.02 versus 1.04 $\pm$ 0.01) and FCFE versus CVX with high temporal resolution (1.03 $\pm$ 0.02 versus 1.04 $\pm$ 0.01) were not significantly different ($P > 0.05$). Eddy current–induced velocity offsets for FCFE, CVX with high spatial resolution, and CVX with high temporal resolution were 0.46 $\pm$ 0.33 cm/s, 0.80 $\pm$ 0.43 cm/s, and 1.01 $\pm$ 0.55 cm/s, respectively. The calculated sequence efficiencies for FCFE, CVX with high spatial resolution,

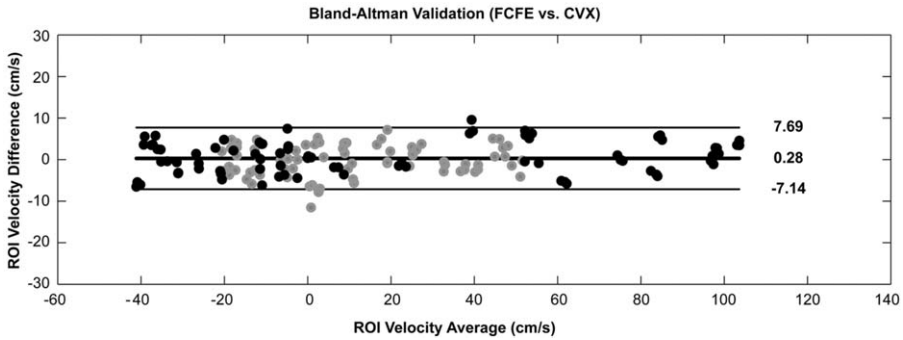

FIG. 3. Bland-Altman analysis of the measured mean velocity within each cardiac phase from the flow phantom experiments measured using FCFE and CVX, each with three repeated measures. The solid lines represent the measurement bias while the dashed lines represent the limits of agreement (95% CI). The gray and black data points represent data from the 150 mL/s and 300 mL/s peak flow rate measurements, respectively. The measurement bias (0.28 cm/s) and 95% CI (−7.14 to 7.69 cm/s) is low, indicating that the measured velocity is the same between the FCFE and CVX sequences for identical PC-MRI protocol parameters.

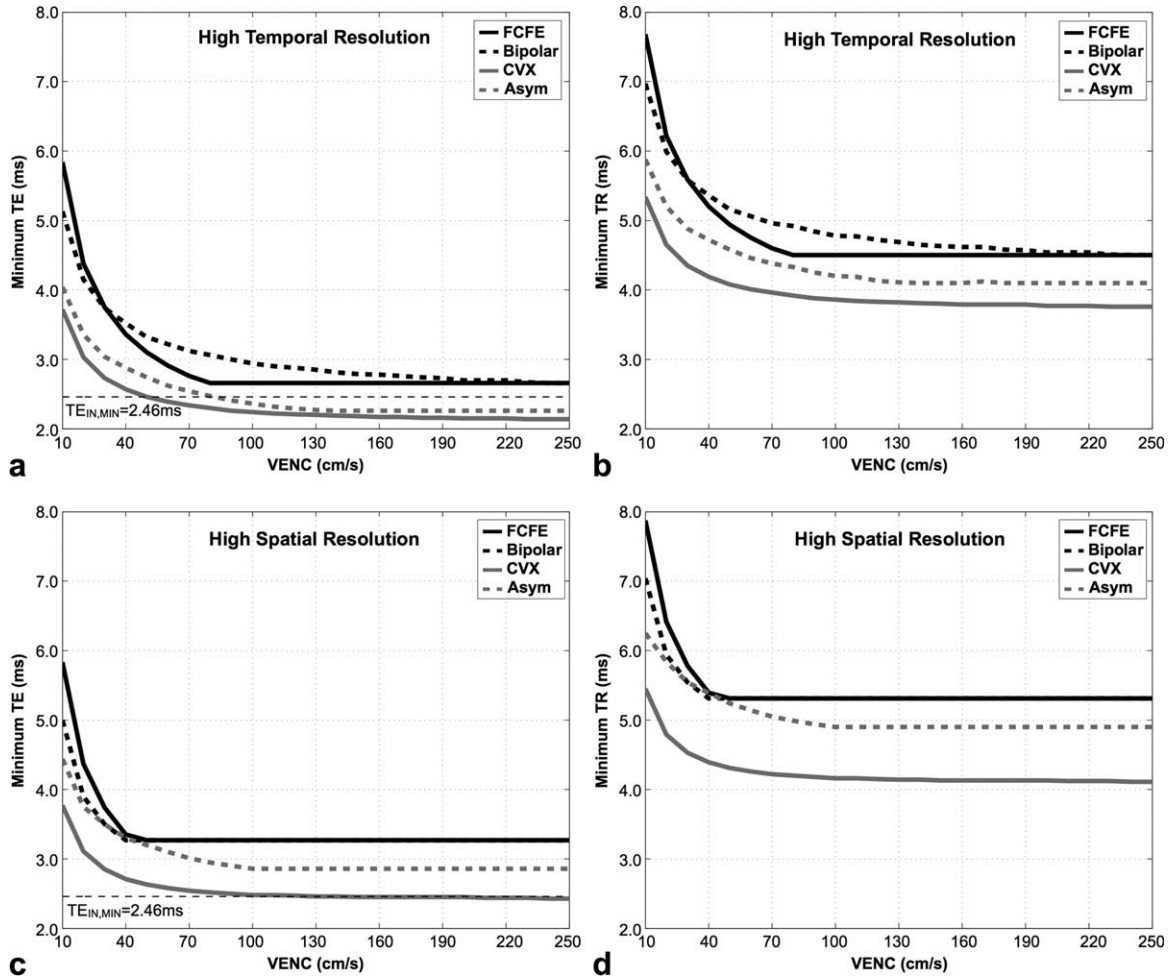

FIG. 4. Minimum achievable TE (**a,c**) and TR (**b,d**) plotted as a function of the target VENC (cm/s) for conventional FCFE velocity-encoding (solid black), bipolar velocity-encoding (black dashed), CVX PC-MRI (solid gray), and asymmetric (Asym) velocity-encoding (dashed gray; see Appendix). The comparisons were conducted for high temporal resolution (a,b) and high spatial resolution (c,d) protocols. All other imaging parameters were held constant (see Methods).

and CVX with high temporal resolution were 17.7%, 30.5%, and 31.4%, respectively. Figure 6 shows representative PC-MRI images and the measured peak velocity profiles from a single volunteer the FCFE and CVX sequences.

DISCUSSION

CVX is used to construct a chemical shift–insensitive, 2D through-plane velocity-encoded PC-MRI sequence with minimum duration gradients for all axes given pulse sequence and hardware constraints. CVX PC-MRI

Table 3
In Vivo PC-MRI Measures of Total Flow and Peak Velocity

	FCFE	CVX Spatial Resolution	CVX Temporal Resolution
Total flow, mL			
aAo	89.0 ± 18.2	95.9 ± 19.4[a]	93.5 ± 17.9[a]
PA	92.6 ± 18.5	100.1 ± 20.1[a]	97.2 ± 18.0[a,b]
RPA	48.1 ± 9.5	52.5 ± 9.9[a]	50.9 ± 9.5[a,b]
LPA	44.3 ± 8.7	47.7 ± 10.2[a]	46.4 ± 9.0[a]
Peak velocity, cm/s			
aAo	117.2 ± 17.2	121.6 ± 15.3[a]	127.3 ± 15.8[a,b]
PA	87.0 ± 11.8	90.0 ± 13.5[a]	95.4 ± 15.4[a,b]
RPA	93.8 ± 15.9	97.1 ± 16.8[a]	104.7 ± 21.7[a,b]
LPA	95.3 ± 18.0	99.7 ± 19.8[a]	107.2 ± 19.9[a,b]

Data are expressed as mean ± standard deviation.
[a]$P < 0.05$ shows a statistical significant difference with FCFE.
[b]$P < 0.05$ shows a statistical significant difference with CVX spatial resolution.

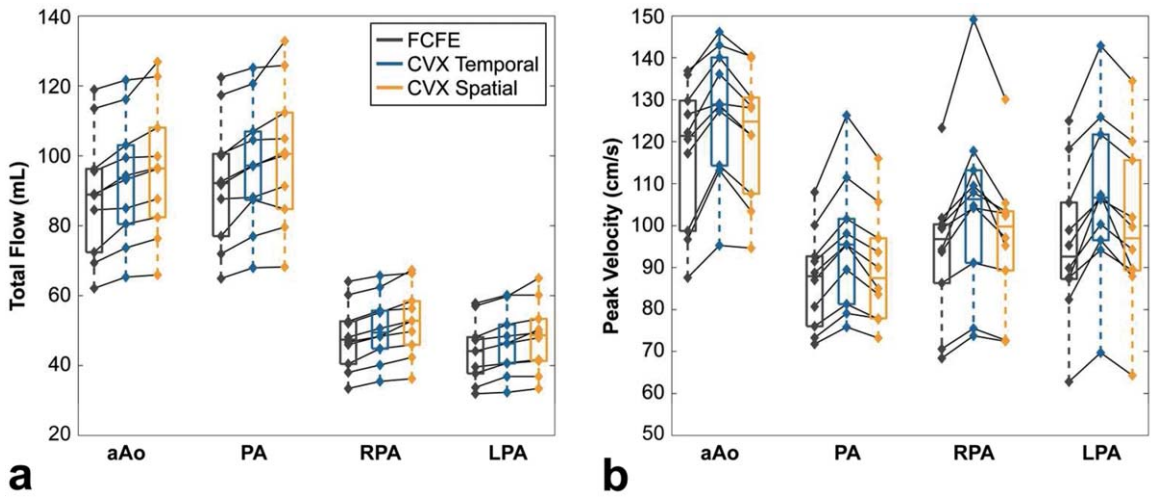

FIG. 5. Total flow (**a**) and peak velocity (**b**) measurements obtained using FCFE (gray), CVX with high spatial resolution (blue), and CVX with high temporal resolution (yellow). Data from each of the 10 volunteers are connected to show that both CVX protocols led to increased measures of total flow and peak velocity compared with FCFE for every volunteer and every region. All data are eddy current–corrected. The box plots show the median and 25th and 75th percentiles; the error bars show the 95% CIs.

provides more accurate measurements of blood flow and peak velocity due to increased sequence efficiency, which affords time-efficient chemical shift insensitivity in addition to increased spatial or temporal resolution.

The low measurement bias and narrow 95% CIs of the Bland-Altman results indicate that flow phantom velocity measurements acquired with CVX PC-MRI are in excellent agreement with conventional FCFE PC-MRI for

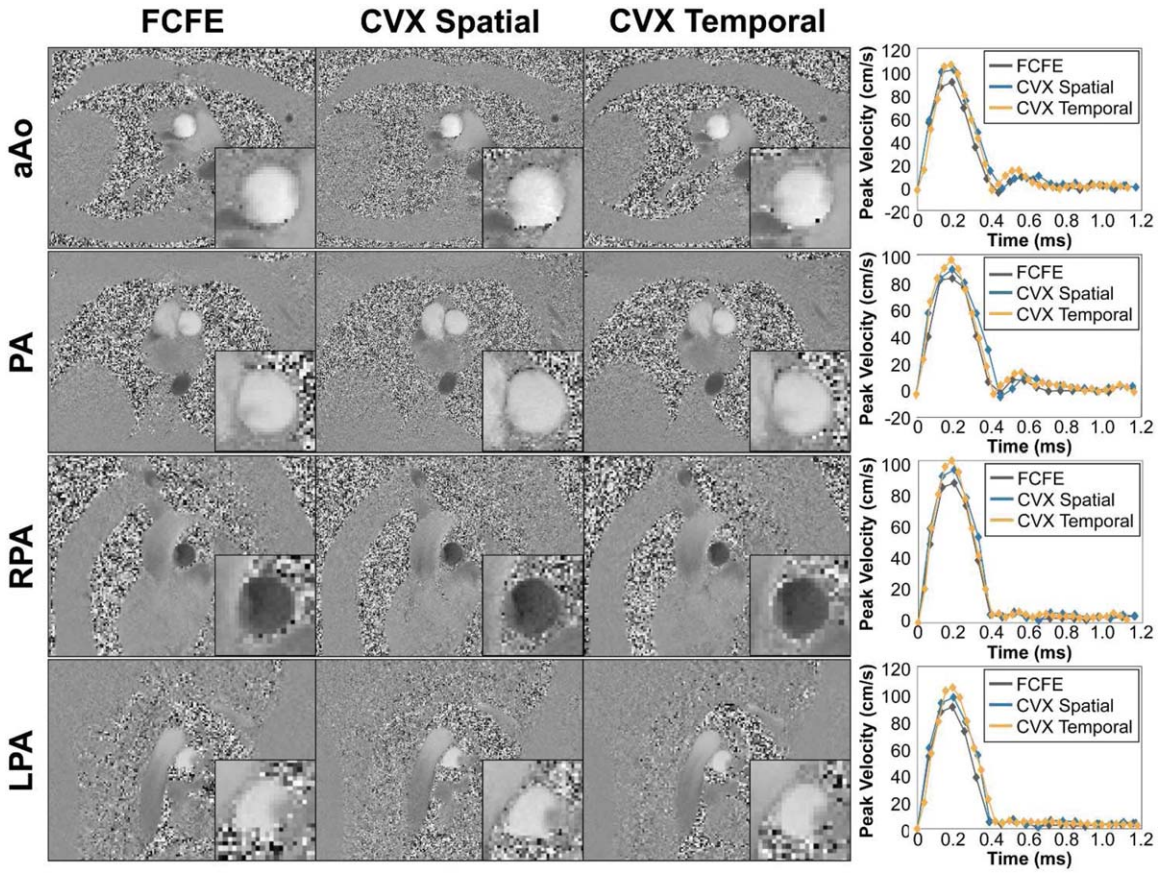

FIG. 6. Representative PC-MRI images and measured peak velocity profiles within the ascending aorta (aAo), main pulmonary artery (PA), right pulmonary artery (RPA), and left pulmonary artery (LPA) from a single volunteer for the FCFE and CVX sequences.

identical scan parameters. Simulations and both flow phantom and in vivo experiments highlight that: 1) increasing spatial resolution leads to larger increases in flow measurements compared with peak velocity measurements; and 2) increasing temporal resolution leads to larger increases in peak velocity measurements than total flow measurements. Nevertheless, further spatiotemporal resolution improvements are needed for flow quantification to achieve <5% measurement errors.

The sequence comparison results show that CVX will always be faster than conventional FCFE or Bipolar, but at the expense of increased sequence complexity. The preclinical evaluation of CVX PC-MRI in normal volunteers resulted in higher measurements of total flow and peak velocity compared with FCFE, which we infer are more accurate from our simulation and flow phantom results. Additionally, in the absence of shunts or regurgitant flow (neither of which is expected within our normal volunteer population), we expect that the measured Qp/Qs ratios be close to 1.05 [accounting for flow loss into the coronary arteries at the level of ascending aorta (42)]. Qp/Qs ratios were close to the expected value of 1.05, and no statistical difference was observed between measures of Qp/Qs between FCFE and CVX. This is due to the fact that FCFE underestimates flow in the ascending aorta and the main pulmonary artery by approximately the same amount. This indicates that blood flow measured with FCFE shows good relative flow agreement when chemical shift effects are mitigated, but lacks absolute flow agreement. CVX PC-MRI therefore represents a more accurate sequence for quantifying blood flow and velocity due to increased spatiotemporal sampling.

Measurements of eddy current–induced velocity offsets for CVX with high spatial and temporal resolution were greater than FCFE. This is likely due to the fact that the CVX sequences uses higher gradient slew rates that may result in higher eddy current–induced velocity offsets. Additionally, dead time exists in the FCFE sequence ($TE_{IN} > TE_{MIN}$), which allows for eddy current fields to dissipate, resulting in reduced eddy current–induced velocity offsets. FCFE was the only sequence that resulted in acceptable (<0.6 cm/s) eddy current–induced velocity offsets before correction (11), which indicates that to obtain the most accurate PC-MRI measurements using CVX, stationary phantom eddy current corrections should be performed.

In order to control for the effects of chemical shift–induced phase errors, all PC-MRI sequences used a high receiver bandwidth and TE_{IN} (8). The reduced gradient durations in CVX PC-MRI allows the use of $TE_{IN,MIN}$ = 2.46 ms at 3T. $TE_{IN,MIN}$ cannot be achieved with the conventional FCFE PC-MRI sequence, thus it is necessary to use the next available TE_{IN} (TE_{IN} = 4.92 ms). This leads to a concomitant increase in TE and TR, which decreases signal-to-noise ratio due to T_2* effects and reduces temporal resolution. Although this derates the FCFE sequence, it also controls for a significant source of error.

For $TE_{IN,MIN}$ protocols, the CVX optimization for Interval 1 (Fig. 1b,c) takes <20 s to arrive at a solution, whereas for TE_{MIN} protocols, for which the search interval (T_L,T_U) is longer, the CVX optimization takes ≈60 s on a MacBook Pro (2.26 Ghz Core 2 Duo with 8 GB RAM). The CVX optimization for Interval 2 takes <18 s to arrive at a solution.

In addition to providing more accurate measures of blood flow and peak velocity with either increased spatial or temporal resolution, CVX also offers nearly double the sequence efficiency compared with FCFE. This is primarily due to a more efficient use of the available gradient hardware and an asymmetric distribution of M_1, but also to a lesser degree due to a reduction in the area of the applied slice select spoiler gradient. CVX with 4π gradient spoiling shortened the spoiling duration by ~0.25 ms compared with CVX with 9π gradient spoiling, which was shorter than FCFE with 9π gradient spoiling by ~0.27 ms.

CVX may prove especially useful for low VENC applications, such as measuring cerebrospinal fluid flow or myocardial velocity mapping. The increased spatial resolution provided by CVX could be useful for measuring blood flow in the small (e.g., carotid or coronary) arteries, while the increased temporal resolution provided by CVX could be useful for measuring high-velocity turbulent jets associated with stenotic and regurgitant valvular disease. Furthermore, instead of increasing spatiotemporal resolution, CVX could be used to reduce scan time, which would be extremely useful for four-dimensional (4D) flow applications. Preliminary estimates indicate 4D flow acquisition times could be reduced by ~33%.

This study has some limitations. The PC-MRI sequences were restricted to the use of TE_{IN} for reduction of chemical shift–induced phase errors. When chemical shift effects are not of a concern, the minimum available TE/TR can be further reduced for CVX, resulting in higher sequence efficiency and the use of higher spatial or temporal resolution. Regardless of chemical shift–induced errors, CVX always provides the shortest TE/TR compared with FCFE, which can be used to increase spatiotemporal resolution or reduce breath-hold time.

Currently, the CVX optimization is conducted offline using MATLAB. This requires that the desired VENC, FOV, matrix size, receiver bandwidth, slice thickness, and RF pulse duration be known a priori. Furthermore, these sequence parameters cannot be altered during a scan, which currently limits the clinical use of the sequence. In addition, based on Equations [5c] and [5d], the current optimization produces a time-efficient solution that works for all slice orientations and does not exceed peripheral nerve simulation limits. However, further incremental improvements may be possible by considering slice-specific physical gradient hardware constraints. Both of the above-mentioned limitations could be overcome by conducting the CVX optimization online. In addition, the use of C++ libraries rather than MATLAB could reduce the time needed for optimization.

CONCLUSIONS

CVX PC-MRI increases sequence efficiency while reducing chemical shift–induced phase errors. This can be used to provide either higher spatial or higher temporal resolution than conventional chemical shift–mitigated PC-MRI methods to provide more accurate measurements of blood flow and peak velocity.

ACKNOWLEDGMENT

We thank Subashini Srinivasan for technical expertise and Gerhard Laub for helpful discussion.

APPENDIX

A fast iterative solution for time-efficient trapezoidal and triangular gradient lobes for a pair of asymmetric velocity-encoding gradients, a flow-compensated readout gradient, and a phase-encoding gradient can be used to determine the upper bound, T_u, for the CVX algorithm or design a sequence that is faster that FCFE or Bipolar.

The gradients along the slice select axis (Fig. 7a,b) must be designed based on the moment constraints detailed in Equation [3a]. In doing so, the velocity-encoding gradient plateau variables (T_1, T_2, T_3, and T_4) can be determined as:

$$T_1 = -\frac{\frac{13G_{VE}^2}{8} - \sqrt{36SR_{VE}^2F_S^2G_S^2 + 72SR_{VE}^2F_SG_S^2R_S + 36SR_{VE}^2F_SG_SR_SG_{VE} + 24SR_{VE}^2F_SR_SG_{VE}^2}}{24SR_{VE}G_{VE}} + \cdots$$
$$\frac{\sqrt{36SR_{VE}^2G_S^2R_S^2 + 36SR_{VE}^2G_SR_S^2G_{VE} - 21SR_{VE}^2R_S^2G_{VE}^2 + 288\Delta M1SR_{VE}^2G_{VE}}}{24SR_{VE}G_{VE}} + \cdots$$
$$\frac{\sqrt{36SR_{VE}F_SG_SG_{VE}^2 - 24SR_{VE}F_SG_{VE}^3 + 36SR_{VE}G_SR_SG_{VE}^2 - 42SR_{VE}R_SG_{VE}^3 + 171G_{VE}^4}}{24SR_{VE}G_{VE}} + \cdots$$
$$\frac{SR_{VE}F_SG_S}{4} + \frac{SR_{VE}G_SR_S}{4} + \frac{SR_{VE}R_SG_{VE}}{8} \quad [12a]$$

$$T_2 = -\frac{\sqrt{6}\sqrt{6SR_{VE}^2F_S^2G_S^2 + 12SR_{VE}^2F_SG_S^2R_S + 6SR_{VE}^2F_SG_SR_SG_{VE} + 2SR_{VE}^2F_SR_SG_{VE}^2}}{12SR_{VE}G_{VE}} + \cdots$$
$$\frac{\sqrt{6}\sqrt{6SR_{VE}^2G_S^2R_S^2 + 6SR_{VE}^2G_SR_S^2G_{VE} - SR_{VE}^2R_S^2G_{VE}^2 - 24SR_{VE}^2T2^2G_{VE}^2 + 24\Delta M1SR_{VE}^2G_{VE}}}{12SR_{VE}G_{VE}} + \cdots$$
$$\frac{\sqrt{6}\sqrt{6SR_{VE}F_SG_SG_{VE}^2 - 2SR_{VE}F_SG_{VE}^3 + 6SR_{VE}G_SR_SG_{VE}^2 - 2SR_{VE}R_SG_{VE}^3 - 72SR_{VE}T2G_{VE}^3}}{12SR_{VE}G_{VE}} - \cdots$$
$$\frac{\sqrt{6}\sqrt{39G_{VE}^4} - 18G_{VE}^2}{12SR_{VE}G_{VE}} \quad [12b]$$

$$T_3 = T_2 - \frac{R_S}{2} + \frac{G_{VE}}{2SR_{VE}} - \frac{F_SG_S}{2G_{VE}} - \frac{G_SR_S}{2G_{VE}} \quad [12c]$$

$$T_4 = T_1 + \frac{G_S(F_S + R_S)}{2G_{VE}} \quad [12d]$$

where the unknown parameters for the velocity-encoding gradients applied along the slice select axis include G_{VE} (maximum gradient amplitude) and SR_{VE}, which is solved for later. Additionally, the known parameters include F_S (slice select gradient plateau duration), G_S (slice select gradient amplitude), R_S (slice select ramp down duration), and ΔM_1.

Next, SR_{VE} is set to $SR_{VE} = SR_{Max}/\sqrt{3}$ and G_{VE} is searched from zero to G_{Max} mT/m in increments of 0.0001 mT/m until a solution set for T_1, T_2, T_3, and T_4 meets the following condition, which ensures the duration of the two velocity encoding waveforms are equal:

$$T_4 + T_1 + R_{VE} - T_3 - T_2| \leq 10\mu s \quad [13]$$

where $R_{VE} = G_{VE}/SR_{VE}$ is the ramp duration of the velocity-encoding gradients and 10 μs represents the gradient sampling duration.

The phase-encoding gradient must have the gradient area described in Equation [6a]a and have the same duration as the velocity-encoding gradients ($T_4 + T_1 + 4R_{VE} + R_S$). With these constraints in mind, a triangular phase encoding gradient can be constructed with ramp duration, R_{PE}, gradient amplitude, G_{PE}, and slew rate, SR_{PE}:

$$R_{PE} = \frac{T_4 + T_1 + 4R_{VE} + R_S}{2} \quad [14a]$$

$$G_{PE} = \frac{\pi(N_y - 1)}{\gamma FOV_y R_{PE}} \quad [14b]$$

$$SR_{PE} = \frac{G_{PE}}{R_{PE}} \quad [14c]$$

A time-efficient flow-compensated readout gradient would have a gradient ramp duration, R_{RO}, based on the maximum available gradient amplitude, G_{RO}, and slew rate, SR_{RO}:

$$G_{RO} = \sqrt{G_{Max}^2 - G_{VE}^2 - G_{PE}^2} \quad [15a]$$

$$SR_{RO} = \sqrt{SR_{Max}^2 - SR_{VE}^2 - SR_{PE}^2} \quad [15b]$$

Taking into account the additional moment constraints required to achieve flow compensation at TE (Eqs. [5a]a,b), the gradient plateau variables in Fig. 7c (T_5 and T_6) can be determined as:

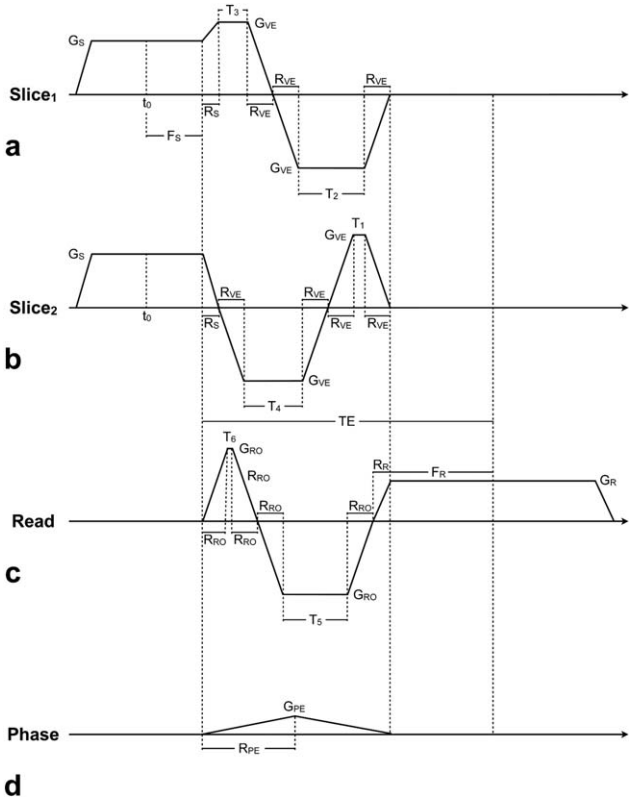

FIG. 7. Pulse sequence diagram of the gradient waveform parameters for a pair of asymmetric velocity-encoding gradients, a flow-compensated readout gradient, and a phase-encoding gradient using triangular and trapezoidal gradient waveforms. The unknown variables T_1, T_2, T_3, T_4, T_5, and T_6 (described in the Appendix) are used to construct initial estimates of the gradient waveforms, which then define the upper bound (T_u) for the CVX optimization.

$$T_5 = \frac{3\sqrt{\frac{G_R^2F_R^2SR_{RO}^2}{2} + \frac{4G_R^2F_RR_RSR_{RO}^2}{3} + \frac{17G_R^2R_R^2SR_{RO}^2}{18} + \frac{G_R^2F_R^2SR_{RO}^2}{2} + \frac{4F_RG_R^3SR_{RO}}{3} + 2G_R^2F_RR_RSR_{RO}^2}}{6G_RSR_{RO}} + \cdots$$
$$\frac{3\sqrt{2G_R^3R_RSR_{RO} + \frac{4G_R^2R_R^2SR_{RO}^2}{3} + \frac{G_R^2R_RSR_{RO}^2}{5} + G_R^4} + SR_{RO}(3G_RF_R + 4G_RR_R) - 9G_R^2}{6G_RSR_{RO}} \quad [16a]$$

$$T_6 = T_5 - \frac{G_R(F_R + R_R)}{2G_{RO}}. \quad [16b]$$

Finally, the flow-compensated readout duration must be equal to the duration of the velocity encoding and phase encode gradients (Fig. 7d). Thus, the entire process is repeated for another value of G_{VE} until the following additional criteria is met:

$$|T_4 + T_1 + 4R_{VE} + R_S - 4R_{RO} - T_5 - T_6 - R_R| \leq 10\mu s \quad [17]$$

The entire process described above takes <1s to arrive at a solution using MATLAB, which makes it an excellent method for assigning the upper bound for the CVX optimization.

REFERENCES

1. Warnes CA, Williams RG, Bashore TM, et al. ACC/AHA 2008 Guidelines for the management of adults with congenital heart disease: executive summary: a report of the American College of Cardiology/American Heart Association Task Force on Practice Guidelines (writing committee to develop guidelines for the management of adults with congenital heart disease). Circulation 2008;118:2395–2451.
2. Geva T. Indications and timing of pulmonary valve replacement after tetralogy of Fallot repair. Semin Thorac Cardiovasc Surg Pediatr Card Surg Annu 2006:11–22.
3. Pennell DJ, Sechtem UP, Higgins CB, Manning WJ, Pohost GM, Rademakers FE, van Rossum AC, Shaw LJ, Yucel EK. Clinical indications for cardiovascular magnetic resonance (CMR): Consensus Panel report. J Cardiovasc Magn Reson 2004;6:727–765.
4. Chernobelsky A, Shubayev O, Comeau CR, Wolff SD. Baseline correction of phase contrast images improves quantification of blood flow in the great vessels. J Cardiovasc Magn Reson 2007;9:681–685.
5. Bernstein MA, Zhou XJ, Polzin JA, King KF, Ganin A, Pelc NJ, Glover GH. Concomitant gradient terms in phase contrast MR: analysis and correction. Magn Reson Med 1998;39:300–308.
6. Markl M, Bammer R, Alley MT, Elkins CJ, Draney MT, Barnett A, Moseley ME, Glover GH, Pelc NJ. Generalized reconstruction of phase contrast MRI: analysis and correction of the effect of gradient field distortions. Magn Reson Med 2003;50:791–801.

7. Bernstein MA, Ikezaki Y. Comparison of phase-difference and complex-difference processing in phase-contrast MR angiography. J Magn Reson Imaging 1991;1:725–729.
8. Middione MJ, Ennis DB. The effects of chemically shifted perivascular fat in quantitative phase contrast MRI. Magn Reson Med 2013;69: 391–401.
9. Tang C, Blatter DD, Parker DL. Accuracy of phase-contrast flow measurements in the presence of partial-volume effects. J Magn Reson Imaging 1993;3:377–385.
10. Laffon E, Lecesne R, De Ledinghen V, Valli N, Couzigou P, Laurent F, Drouillard J, Ducassou D, Barat JL. Segmented 5 versus nonsegmented flow quantitation: comparison of portal vein flow measurements. Invest Radiol 1999;34:176–180.
11. Gatehouse PD, Rolf MP, Graves MJ, et al. Flow measurement by cardiovascular magnetic resonance: a multi-centre multi-vendor study of background phase offset errors that can compromise the accuracy of derived regurgitant or shunt flow measurements. J Cardiovasc Magn Reson 2010;12:5.
12. Middione MJ, Ennis DB. Velocity encoding with the slice select refocusing gradient for faster imaging and reduced chemical shift-induced phase errors. Magn Reson Med 2014;71:2014–2023.
13. Eichenberger AC, Schwitter J, McKinnon GC, Debatin JF, von Schulthess GK. Phase-contrast echo-planar MR imaging: real-time quantification of flow and velocity patterns in the thoracic vessels induced by Valsalva's maneuver. J Magn Reson Imaging 1995;5:648–655.
14. Pike GB, Meyer CH, Brosnan TJ, Pelc NJ. Magnetic resonance velocity imaging using a fast spiral phase contrast sequence. Magn Reson Med 1994;32:476–483.
15. Thompson RB, McVeigh ER. Flow-gated phase-contrast MRI using radial acquisitions. Magn Reson Med 2004;52:598–604.
16. Griswold MA, Jakob PM, Heidemann RM, Nittka M, Jellus V, Wang J, Kiefer B, Haase A. Generalized autocalibrating partially parallel acquisitions (GRAPPA). Magn Reson Med 2002;47:1202–1210.
17. Pruessmann KP, Weiger M, Scheidegger MB, Boesiger P. SENSE: sensitivity encoding for fast MRI. Magn Reson Med 1999;42:952–962.
18. Foo TK, Bernstein MA, Aisen AM, Hernandez RJ, Collick BD, Bernstein T. Improved ejection fraction and flow velocity estimates with use of view sharing and uniform repetition time excitation with fast cardiac techniques. Radiology 1995;195:471–478.
19. Markl M, Hennig J. Phase contrast MRI with improved temporal resolution by view sharing: k-space related velocity mapping properties. Magn Reson Imaging 2001;19:669–676.
20. Lin HY, Bender JA, Ding Y, Chung YC, Hinton AM, Pennell ML, Whitehead KK, Raman SV, Simonetti OP. Shared velocity encoding: a method to improve the temporal resolution of phase-contrast velocity measurements. Magn Reson Med 2012;68:703–710.
21. McGibney G, Smith MR, Nichols ST, Crawley A. Quantitative evaluation of several partial Fourier reconstruction algorithms used in MRI. Magn Reson Med 1993;30:51–59.
22. Lustig M, Donoho D, Pauly JM. Sparse MRI: the application of compressed sensing for rapid MR imaging. Magn Reson Med 2007;58: 1182–1195.
23. Baltes C, Kozerke S, Hansen MS, Pruessmann KP, Tsao J, Boesiger P. Accelerating cine phase-contrast flow measurements using k-t BLAST and k-t SENSE. Magn Reson Med 2005;54:1430–1438.
24. Bernstein MA, Shimakawa A, Pelc NJ. Minimizing TE in moment-nulled or flow-encoded two- and three-dimensional gradient-echo imaging. J Magn Reson Imaging 1992;2:583–588.
25. Bolster BD Jr, Atalar E. Minimizing dead-periods in flow-encoded or -compensated pulse sequences while imaging in oblique planes. J Magn Reson Imaging 1999;10:183–192.
26. Atalar E, McVeigh ER. Minimization of dead-periods in MRI pulse sequences for imaging oblique planes. Magn Reson Med 1994;32:773–777.
27. Derbyshire JA, Herzka DA, McVeigh ER, Lederman RJ. Efficient implementation of hardware-optimized gradient sequences for real-time imaging. Magn Reson Med 2010;64:1814–1820.
28. Hargreaves BA, Nishimura DG, Conolly SM. Time-optimal multidimensional gradient waveform design for rapid imaging. Magn Reson Med 2004;51:81–92.
29. Bryant DJ, Payne JA, Firmin DN, Longmore DB. Measurement of flow with NMR imaging using a gradient pulse and phase difference technique. J Comput Assist Tomogr 1984;8:588–593.
30. Nayler GL, Firmin DN, Longmore DB. Blood flow imaging by cine magnetic resonance. J Comput Assist Tomogr 1986;10:715–722.
31. Axel L, Morton D. MR flow imaging by velocity-compensated/uncompensated difference images. J Comput Assist Tomogr 1987;11:31–34.
32. van Dijk P. Direct cardiac NMR imaging of heart wall and blood flow velocity. J Comput Assist Tomogr 1984;8:429–436.
33. Zou Y, Middione MJ, Srinivasan S, Ennis DB.Analysis of Gradient Spoiling in Phase Contrast. In Proceedings of the 21st Annual Meeting of ISMRM, Salt Lake City, Utah, USA 2013. p. 4436.
34. Blondel VD, Boyd SP, Kimura H, editors. Recent advances in learning and control. London, England: Springer-Verlag, 2008.
35. Grant M, Boyd SP.CVX: Matlab software for disciplined convex programming, version 2.0 beta. http://cvxr.com/cvx. Published September 2012. Updated June 2013. Accessed August 12, 2013.
36. Boesch C, Gruetter R, Martin E. Temporal and spatial analysis of fields generated by eddy currents in superconducting magnets: optimization of corrections and quantitative characterization of magnet/gradient systems. Magn Reson Med 1991;20:268–284.
37. Atkinson DJ, Edelman RR. Cineangiography of the heart in a single breath hold with a segmented turboFLASH sequence. Radiology 1991;178:357–360.
38. Gatehouse PD, Rolf MP, Bloch KM, Graves MJ, Kilner PJ, Firmin DN, Hofman MB. A multi-center inter-manufacturer study of the temporal stability of phase-contrast velocity mapping background offset errors. J Cardiovasc Magn Reson 2012;14:72.
39. Bland JM, Altman DG. Statistical methods for assessing agreement between two methods of clinical measurement. Lancet 1986;1:307–310.
40. Parker DL, Gullberg GT. Signal-to-noise efficiency in magnetic resonance imaging. Med Phys 1990;17:250–257.
41. Reeder SB, McVeigh ER. The effect of high performance gradients on fast gradient echo imaging. Magn Reson Med 1994;32:612–621.
42. Ganong WF. Review of medical physiology. 22nd edition. New York: Lange Medical Books/ McGraw-Hill; 2005.